RSC Advances

ROYAL SOCIETY OF CHEMISTRY

www.rsc.org/advances

Journal Name

RSCPublishing

ARTICLE

Highly sensitive and selective detection of mercury ions based on Up-conversion FRET from $NaYF_4$: Yb^{3+}/Er^{3+} Nanophosphor to CdTe Quantum Dots

Cite this: DOI: 10.1039/x0xx00000x

Received 00th January 2012,
Accepted 00th January 2012

DOI: 10.1039/x0xx00000x

www.rsc.org/

Shaobo Cui[a, b], Sai Xu[a], Hongwei Song*[a], Wen Xu[a], Xu Chen[a], Donglei Zhou[a], Ze Yin[a], Wei Han*[b]

Abstract

The detection of Hg^{2+} has attracted considerable attention because of the serious health and environmental problems caused by it. There has been progress in the development of fluorescence biosensors based on quantum dots (QDs) for the detection of Hg^{2+}. However, most of them are valid only in aqueous solution rather than in human serum due to the influence of protein autofluorescence in serum excited by ultraviolet or visible light. Herein, we designed and synthesized a novel $NaYF_4$:Yb^{3+}, Er^{3+} upconversion nanoparticles (UCNPs)/CdTe QDs composite probe for Hg^{2+} detection. The $NaYF_4$:Yb^{3+}, Er^{3+} UCNPs were synthesized via a solvothermal method. By grafting CdTe QDs probe onto the surface of $NaYF_4$:Yb^{3+}, Er^{3+} UCNPs, a fluorescence resonance energy transfer (FRET) biosensor for determination of Hg^{2+} ions was obtained under the pumping of 980 nm infrared light, which was capable of overcoming autoluminescence from serum. The spectral response towards Hg^{2+} suggested that the fluorescence intensity of the QDs reduced linearly with the increasing Hg^{2+} concentration. The sensor showed high selectivity, a low detection limit of 15 nM and good linear Stern-Volmer characteristics, both in the buffer and serum. This biosensor has great potential for real application of Hg^{2+} detection in biological and analytical fields.

1. Introduction

As well-known health threat to human being as well as many animal species, mercury and its complexes are considered as unpopular matters due to their participation in many biological processes.[1,2] Many vital organs such as human heart, kidney, stomach and intestines can be poisoned and damaged when the Hg^{2+} concentration reaches a level of 25 nM.[3] The excess Hg^{2+} in human body can initiate a series of diseases including nosebleed, headache, nerve disorder, perforation of stomach, intestines septum and even acute renal failure.[4] The increasing Hg^{2+} contamination in our living environment and ecosystem has created significant concerns. From the viewpoint of environment protection and health concerns, developing an effective method for the sensitive detection of trace amount of Hg^{2+} is very important and has attracted a significant amount of attention.[5]

A variety of traditional methods including atomic absorption spectrometry, atomic fluorescence spectrometry, inductively coupled plasma mass spectroscopy, X-ray absorption spectrometry and electrochemical method have been widely used for mercury ions detection.[6-9] However, these methods require expensive instruments and complicated sample preparation process. In order to overcome these drawbacks, it is highly desirable to develop facile, economical and rapid methodologies with favorable sensitivity and selectivity for mercury detection. Relative to the above methods, the fluorescence method has the advantages of higher sensitivity, simplicity and lower cost for the monitoring of metal ions, which translates molecular recognition information into tangible fluorescence signals. In the past years, fluorescent probes for Hg^{2+} was usually based on organic dyes, noble metal ions and DNA, via Hg^{2+}-induced changes in fluorescence, has abstracted much attention

and become a very active field of research.[10,11] Although progress in developing these methods has occurred, problems remain in applying them to biomonitoring. For instance, organic luminescence dyes are photo-bleached after continuous irradiation by ultraviolet or visible light, and the expensive price of noble metal ions lead to the rise cost of preparation and experiment. Recently, quantum dots (QDs) have become a promising fluorescence probes for mercury detection with the advantage of high sensitivity, simplicity and low cost because of the attractive optical properties, including tunable emission spectra, excellent photochemical stability. For instance, Ding et al. prepared cysteamine capped CdTe QDs to detect Hg^{2+}. The results show the detection of Hg^{2+} based QDs exhibited excellent sensitivity due to the specific and strong affinity of ligands capped on the QDs with Hg^{2+} and the unique luminescence properties of QDs.[12] However, this method is valid in aqueous solution rather than in human serum. The porphyrin and carotenoids in the serum can be excited by visible light and emit fluorescence ranging of 500-600 nm, thus influence detection of Hg^{2+}.[13]

On the other hand, rare earth(RE)-activated UCNPs can convert infrared light to visible through two-photon or multi-photon processes via intermediate states.[14] This unique mechanism allows them to display some special advantages in bio-application, such as a large anti-stokes shift of several hundred nanometers, drastically improving signal-to-noise ratio and reducing background signals owing to the autofluorescence of the other biofluorescent components not being excited with NIR radiation, [15] remarkable light penetration depth in tissue,[16] less harm to cells and tissues in vitro or in vivo, [17] and no photobleaching.[18,19] Many investigation using UCNPs as bio-imaging or bio-detection have been reported due to these advantages.[20-25] However, work related to the detection of Hg^{2+} using $NaYF_4$:Yb^{3+}, Er^{3+} UCNPs/CdTe QDs nanocomposite as Hg^{2+} sensor has not been reported yet. It is expected that the Hg^{2+} probe based on $NaYF_4$:Yb^{3+}, Er^{3+} UCNPs/CdTe QDs nanocomposite can avoid background florescence in the serum.

Guided by above considerations, in this paper, we devised and prepared $NaYF_4$:Yb^{3+}, Er^{3+} UCNPs/CdTe QDs nanocomposite as Hg^{2+} sensor. The hybrid can maintain the sensitivity of CdTe QDs to Hg^{2+}, and through the FRET from $NaYF_4$:Yb^{3+}, Er^{3+} UCNPs to CdTe QDs, it is promised to detect Hg^{2+} under the excitation of infrared light, which can avoid background florescence of serum. The principle of upconversion FRET mercury-ion detection by employing UCNPs as energy donors and QDs as an energy acceptor is illustrated in Scheme1. The central wavelength of the absorption band of the QDs locates at 547 nm, which mainly overlaps with the 546 nm emission of $NaYF_4$:Yb^{3+}, Er^{3+} UCNPs. As CdTe QDs was electrostatically absorbed on the surface of the $NaYF_4$:Yb^{3+}, Er^{3+} UCNPs, an efficient FRET from UCNPs to QDs was realized when UCNPs was excited by 980 nm light. Because of their small size and high surface area-to-volume ratio, the photoluminescence of QDs is very sensitive to the surface states. After adding the Hg^{2+} ions, the surface states of QDs changed due to the specific interaction between Hg^{2+} and carboxyl on the surface of QDs, leading to fluorescence quenching of QDs. Ultimately, the Hg^{2+} ions were detected quantitatively through the spectrum change of QDs.

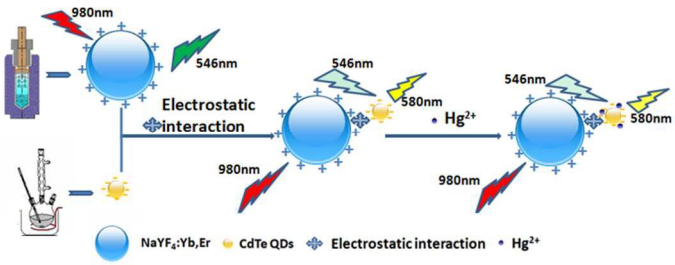

Scheme 1 Principle of upconversion Hg^{2+} ions FRET detection by employing UCNPs as donor and QDs as acceptor.

2. Experimental section

2.1 Synthesis of PEI-modified $NaYF_4$:Yb^{3+}, Er^{3+} UCNPs

PEI-modified water-soluble $NaYF_4$:Yb^{3+}, Er^{3+} UCNPs were synthesized via a solvothermal method following a procedure reported by Liu et al.[26] Briefly, NaCl(2.5 mmol), PEI(0.4 g), $Y(NO_3)$(0.77 mmol), $Yb(NO_3)$(0.2 mmol), and $Er(NO_3)$(0.03 mmol) were dissolved in ethylene glycol(15 mL) under vigorous stirring. After the solution became transparent, NH_4F (4 mmol) in ethylene glycol (10 mL) was dropwise added to the solution under vigorous stirring. After stirring for another 10 min, the entire mixture solution was transferred into a 25 mL Teflon-lined stainless steel autoclave. The autoclave was sealed and heated under 200℃ for 2 h. After the autoclave was cooled down to room temperature naturally, $NaYF_4$:Yb^{3+}, Er^{3+} UCNPs were collected by centrifugation and washed with deionized water and alcohol three times.

2.2 Preparation of water-soluble CdTe QDs

Stable water-solution CdTe QDs were prepared as described in previous papers.[27] Briefly, cadmium chloride ($CdCl_2 \cdot 2.5H_20$, 0.04 M, 16 mL) was diluted to 200 mL in a one-necked flask, and trisodium citrate dehydrate(400 mg), Na_2TeO_3(0.01 M, 4 mL), MSA(200 mg), and sodium borohydride($NaBH_4$, 400mg) were added with stirring. When the color of the solution changed to green, the flask was attached to a condenser and refluxed under open-air conditions for 6 h. The resulting CdTe QDs were washed with ethanol and separated by centrifugation. Finally, the prepared CdTe QDs were dispersed in water.

2.3 Detection of FRET process from UCNPs to QDs

A specified concentration of UCNPs was transferred to a cuvette, and then different concentration of QDs was added to the solution. After 10 min incubation at room temperature, the luminescence spectra were measured with a photomultiplier combined with a monochromator for signal collection from 350 nm to 750 nm. A continuous 980 nm diode laser was used to pump the samples to investigate steady-state spectra. In the measurements of luminescent dynamics, the samples were pumped by a laser system consisting of a Nd:YAG pumping laser (1064 nm), the third-order harmonic generator (355 nm) and a tunable optical parameter

oscillator (OPO, Continuum Precision II 8000). Pulse duration was 10 ns, repetition frequency 10 Hz, and line width 4–7 cm^{-1}.

2.4 Sensitivity and selectivity of Hg^{2+} detection in PBS buffer

$HgSO_4$ was used for the Hg^{2+}-sensitivity studies. UCNPs/CdTe QDs nanocomposites were mixed in the buffer after 10 min incubation at room temperature. Different concentrations of Hg^{2+} were added to the mixture solution, and then emission spectra were measured with the same equipment described in section 2.3. To determine FRET probe selectivity, various ions, including Mg^{2+}, K^+, Na^+, Cl^-, Zn^{2+}, Cu^{2+}, Cd^{2+}, Ag^+, Al^{3+} and Ni^{2+} were prepared at a concentration of 0.5 mM. The solutions above and 1μM of Hg^{2+} solution were added to the mixture individually and changes in fluorescence were monitored.

In the control experiment, the QD solution was transferred to a cuvette, and then a specific concentration of Hg^{2+} was added. The emission spectra were measured under 365 nm excitation with a SENS-9000 spectrometer.

2.5 Detection of Hg^{2+} in real samples

The UCNPs/CdTe QDs nanocomposites were incubated in the serum (0.1 g/mL). After 10 min incubation at room temperature, different concentration of Hg^{2+} was added to the mixture solution. The emission spectra were measured with the same equipment as the detection process in the buffer.

In the control experiment, QDs were mixed in the serum, and then different concentration of Hg^{2+} was added; the emission spectra were measured with the same equipment as the detection process in the buffer.

3. Characterization

Transmission electron micrographs were obtained with a Hitachi H-800 transmission electron microscope (TEM) operating at an acceleration voltage of 200 kV. High-resolution transmission electron microscope (HR-TEM) images and elemental mapping were recorded on a FEI Tecnai G2 S-Twin microscope operated with an acceleration voltage of 200 kV. The crystalline structure of the samples was characterized by X-ray diffraction (XRD) (RigakuD/max-rA power diffractometer using Cu-KR radiation (λ= 1.54178 Å). Ultraviolet-visible (UV-vis) absorption spectra were measured with a Shimadzu UV-3101PC UV-vis scanning spectrophotometer ranging of 200–1100 nm. The emission spectra were recorded at room temperature using a HitachiF-4500 spectrophotometer. The luminescence dynamics were studied using a laser system consisting of a Nd:YAG pumping laser (1064 nm), a third-order harmonic generator (355 nm), and a tunable optical parameter oscillator (OPO, Continuum Precision II 8000). Pulse duration was 10 ns, repetition frequency 10 Hz, and line width 4–7 cm^{-1}.

4. Results and discussion

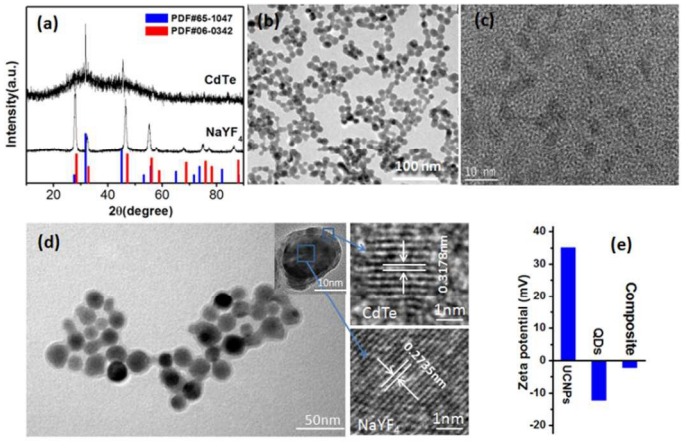

Fig. 1 (a) XRD patterns of the $NaYF_4$ UCNPs and CdTe QDs. (b) TEM image of $NaYF_4$ UCNPs. (c) HR-TEM image of CdTe QDs. (d) TEM image of CdTe QDs adsorbed on the surface of UCNPs, HR-TEM of CdTe and $NaYF_4$ (inset: TEM image of CdTe QDs adsorbed on the surface of UCNPs). (e) Zeta potential of $NaYF_4$ UCNPs, CdTe QDs and composite.

4.1 Morphology and structure of $NaYF_4$:Yb,Er UCNPs and CdTe QDs

The UCNPs and QDs could be well-dispersed in water to form stable colloidal solutions directly without further surface modification. Fig. 1(a) exhibits XRD patterns of the $NaYF_4$: Yb,Er UCNPs and CdTe QDs. From the XRD patterns it can be observed that all the diffraction peaks are indexed to the cubic phase structure of $NaYF_4$ crystals, which is in accordance with JCPDS card no. 77-2042, suggesting high product crystallinity. The mean crystallite size of the product was estimated from the XRD pattern according to the Scherrer formula $D = K\lambda/\beta\cos\theta$, where λ is the X-ray wavelength (0.15406 nm), βis the full-width at half-maximum, θ is the diffraction angle, and K is a constant (0.89).[28] The estimated mean crystallite size of $NaYF_4$ crystals is 16.9 nm. It can be seen from the XRD patterns of the CdTe QDs that all the diffraction peaks can be indexed in accordance with the cubic phase CdTe QDs (JCPDS:65-1047), indicating that the prepared sample is pure in phase. Fig. 1(b) shows the TEM image of spherical morphology of the $NaYF_4$ UCNPs. It is with an average diameter of 17.1 nm, which is well accordance with the theoretical calculation. Fig. 1(c) shows the HR-TEM picture of the water-dispersed CdTe QDs, in which the average size of pristine CdTe QDs was estimated to be 3.5 nm. Fig. 1(d) demonstrates the HR-TEM image of the $NaYF_4$: Yb^{3+}, Er^{3+}/CdTe QDs composites, CdTe QDs and $NaYF_4$: Yb^{3+}, Er^{3+} UCNPs. It can be seen that the CdTe QDs were adsorbed on the surface of $NaYF_4$ UNCPs. The lattice spacing of the QDs was 0.3178 nm, corresponding to the (002) planes in the cubic phase of CdTe QDs, and the lattice spacing of the $NaYF_4$ UCNPs was 0.2735 nm, corresponding to the (200) planes in the cubic phase of $NaYF_4$

UCNPs. Fig. 1(e) shows the zeta potential between the $NaYF_4$ UNCPs, CdTe QDs and composite. It can be seen that $NaYF_4$ UNCPs have positive charge (ζpotential=+35.3 mV), CdTe QDs have negative (ζpotential=-12.34 mV) and the composite have negative charge (ζpotential=-3.5 mV). The opposite potential contributes to strong electrostatic interaction between UCNPs and QDs. Fig. S2 displays the TEM image and elemental mapping of $NaYF_4$/CdTe QDs. The EDX analysis indicates that the CdTe QDs were successfully absorbed on the surface of $NaYF_4$ UCNPs, and the concentration of QDs is determined to be 32%, which is a little bit smaller than its starting concentration (45%). The formation of the CdTe-surrounded $NaYF_4$ structure is attributed to not only the electrostatic interaction between UCNPs and QDs, but also the large difference in size of CdTe QDs and $NaYF_4$ UCNPs.[29] The size of CdTe QDs is much smaller than that of $NaYF_4$, leading to CdTe QDs adsorbed on $NaYF_4$ rather than in reverse. As mentioned above, it can be confirmed that the CdTe QDs were successfully absorbed on the surface of $NaYF_4$ UCNPs.

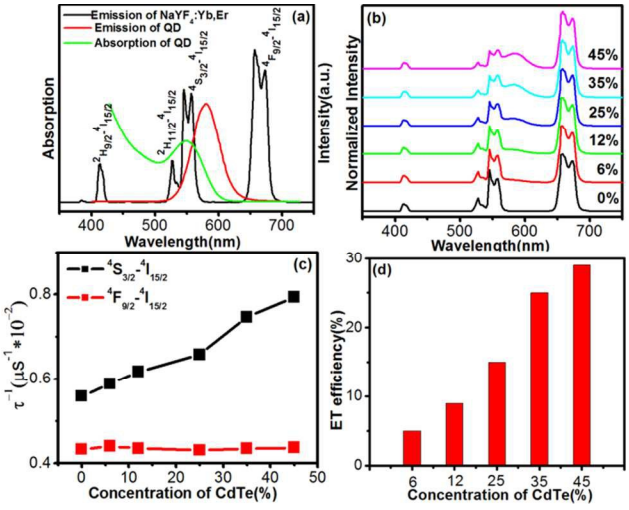

Fig.2 (a) Emission spectrum (black line) of $NaYF_4$: Yb^{3+}, Er^{3+} UCNPs; absorption (green line) and emission (red line) spectra of CdTe QD1. (b) FRET spectra of mixture solution with different QD1 concentrations excited at 980 nm. (c) Inverse of the $^4S_{3/2}$, $^4F_{9/2}$-$^4I_{15/2}$ transition decay time at different QD1 concentration under 980 nm light excitation. (d) Energy transfer (ET) efficiency from UCNPs to QD1 versus different concentrations of QD1.

4.2 FRET process from UCNPs to QDs

FRET is a non-radiation process characterized by energy transfer between an excited donor and an acceptor through long-range dipole-dipole interaction, which is widely used as a spectroscopic ruler in biosensing and bioimaging.[25] An efficient FRET process requires the following: (1) the acceptor absorption spectrum overlaps with the donor emission spectrum; and (2) the distance between a donor and an acceptor must be linked in close proximity, typically less than a few nanometers.[30] Fig. 2(a) shows the upconversion emission spectrum of $NaYF_4$: Yb^{3+}, Er^{3+} nanoparticles under 980 nm excitation, absorption and emission spectra of the CdTe QD1. In the emissions of the Er^{3+} ions, the $^2H_{9/2}$, $^2H_{11/2}$, $^4S_{3/2}$, and $^4F_{9/2}$-$^4I_{15/2}$ transitions were observed, locating at 412, 526, 546, and 658 nm, respectively. The central wavelength of the absorption band of the QD1 locates at 547 nm, which exactly overlaps with the 546 nm ($^4S_{3/2}$-$^4I_{15/2}$) emission of $NaYF_4$: Yb^{3+}, Er^{3+} UCNPs. The emission band of the QD1 locates at 580 nm, which corresponds to an orange color, does not overlap with the emission of Er^{3+} ions. The QDs emission originates from the radiation recombination of electrons and holes trapped in defect states.[31] There are sufficient conditions for UCNPs-QDs non-radiative energy transfer (NRET) to take place because the green luminescence of the donor (Er^{3+}) overlaps with the strong absorption band of the acceptor (CdTe). Another important reason that CdTe was selected as the FRET acceptor is that the UCNPs can be excited using an NIR laser at 980 nm where CdTe cannot be photo-excited, thereby avoiding CdTe excitation by external light and eliminating luminescent background interference.

The emission spectra of Er^{3+} ions versus the concentration of the QD1 in the $NaYF_4$: Yb^{3+}, Er^{3+}/CdTe QD1 mixture solution under the excitation of 980 nm laser diode are shown in Fig. 2(b), the emission from $^4F_{9/2}$-$^4I_{15/2}$ transitions around 658 nm situates relatively far away from the absorption and emission spectra of the CdTe QD1 and is almost unchanged, so it is normalized for comparison. It can be seen that the emission band of the QD1 gradually increases with the addition of QD1, while the green emission at 530-570 nm of Er^{3+} gradually decreases, indicating the appearance of FRET from Er^{3+} to CdTe QD1. The blue and red emission at 400-430 and 635-670 nm are almost unchanged.

To further confirm the FRET process, the decay dynamics for $^4S_{3/2}$-$^4I_{15/2}$ and $^4F_{9/2}$-$^4I_{15/2}$ transition processes of Er^{3+} with different QD1 concentration were investigated. All the dynamic curves exhibited exponential decay (as shown in Fig. S3, S4). According to the inverse of $^4S_{3/2}$-$^4I_{15/2}$ and $^4F_{9/2}$-$^4I_{15/2}$ transition decay time constant as shown in Fig. 2(c), It can be clearly seen that with increasing concentration of QD1 from 0 to 45%, the decay rate for $^4S_{3/2}$-$^4I_{15/2}$ transition of Er^{3+} linearly increases from 0.56 μs^{-1} to 0.78 μs^{-1}, which is evidence for NRET from $^4S_{3/2}$ of Er^{3+} to the QD1. Meanwhile, the decay time for $^4F_{9/2}$-$^4I_{15/2}$ transition of Er^{3+} remains almost unchanged with concentration variation, which means that there is no energy transfer from $^4F_{9/2}$ of Er^{3+} to QD1. The energy transfer efficiency from $^4S_{3/2}$ of Er^{3+} to QD1 can be calculated as follows:[15]

$$\eta = 1 - \tau_D^1/\tau_D$$

where τ_D^1 and τ_D represent the decay lifetime of $^4S_{3/2}$ level of Er^{3+} in the presence and absence of QD1, respectively. According to the equation, the calculated energy transfer efficiency from UCNPs to QD1 as a function of the amount of the QD1 is shown in Fig. 2(d). It can be seen that the energy transfer efficiency gradually increases with increasing the concentration of QD1. It reaches 28.3% when the concentration of QD1 is 45%. It should be noted that there were no large aggregates during the mixing process with the

increasing QDs concentration in water or buffer solution, Moreover, after keeping more than one week, the colloidal had no aggregation, indicating its excellent stability, as seen in the photograph of the UCNP and QDs complex (QDs concentration is 45%, Fig. S5)

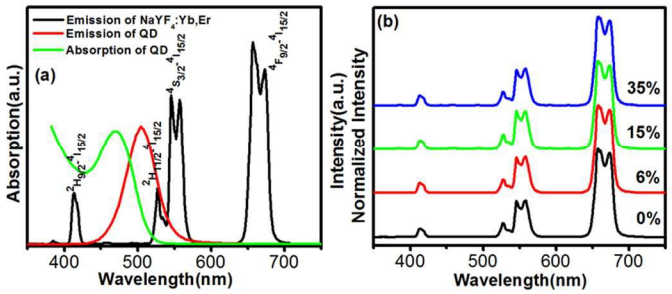

Fig.3 (a) Emission spectrum (black line) of $NaYF_4$: Yb^{3+}, Er^{3+} UCNPs; absorption (green line) and emission (red line) spectra of CdTe QD2. (b) FRET spectra of mixture solution with different QD2 concentrations excited at 980 nm.

As a contrast, CdTe QD2 with the central absorption band at 465 nm was synthesized. From Fig. 3(a) it can be seen that the central wavelength of the absorption band for QD2 does not overlap with any emission of $NaYF_4$: Yb^{3+}, Er^{3+} UCNPs. The emission spectra of Er^{3+} ions versus the concentration of the QD2 in the $NaYF_4$: Yb^{3+}, Er^{3+}/CdTe QD2 mixture solution under the excitation at 980 nm was shown in Fig. 3(b). While exciting Er^{3+} ions to excited states, no emission from CdTe was identified, implying FRET did not happen. The decay dynamics for $^4S_{3/2}$-$^4I_{15/2}$ and $^4F_{9/2}$-$^4I_{15/2}$ transition processes of Er^{3+} with different QD1 concentration were investigated. All the dynamic curves exhibited exponential decay (as shown in Fig. S6, S7), the decay rates of $^4S_{3/2}$-$^4I_{15/2}$ and $^4F_{9/2}$-$^4I_{15/2}$ of Er^{3+} transition on concentration of QD2 were shown in Fig. S8. The results indicate the decay rates for $^4S_{3/2}$-$^4I_{15/2}$ and $^4F_{9/2}$-$^4I_{15/2}$ of Er^{3+} almost unchanged. This further means that there is no energy transfer from $NaYF_4$: Yb^{3+}, Er^{3+} to QD2.

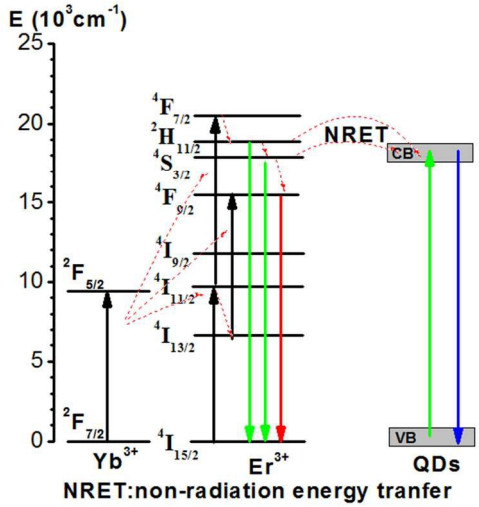

Fig.4 Schematic for the energy transfer process from $NaYF_4$: Yb^{3+}, Er^{3+} UCNPs to CdTe QDs.

The schematic for the upconversion luminescence and energy transfer processes of $NaYF_4$: Yb^{3+}, Er^{3+} /CdTe QDs composites is illustrated in Fig. 4; As shown in Fig. 4, under the pumping of a 980 nm light, the excited states of Er^{3+} ions ($^2H_{11/2}$, $^4S_{3/2}$) as well as $^4F_{9/2}$ are populated through two-step energy transfer processes from Yb^{3+} to Er^{3+} ions. The transitions of $^2H_{11/2}$, $^4S_{3/2}$-$^4I_{15/2}$ match well with the energy gap between the conduction band (CB) and valance band (VB) of the CdTe QDs, resulting in the NRET from UCNPs to QDs.

4.3 Fluorescence response characteristics of FRET probe for Hg^{2+} detection

In the Hg^{2+} sensing system, we chose UCNPs as the energy donors, which can drastically improve signal-to-noise ratio and reduce background signals owing to the autofluorescence of the other biofluorescent components not being excited with NIR radiation, to improve the linearity and accuracy of detection. With the addition of CdTe QDs to the UCNPs, excitation of $NaYF_4$:Yb^{3+}, Er^{3+} UCNPs triggers energy transfer from Er^{3+} to CdTe QDs within a given proximity through electrostatic interaction, and results in emission from QDs at 580 nm, and the weakening of $^2H_{11/2}$,$^4S_{3/2}$-$^4I_{15/2}$ transitions for Er^{3+}. The carboxyl capping layer was crucial for CdTe QD luminescent efficiency and water stability. Thus, as adding the Hg^{2+} ions, the surface states of QDs changed with the addition of Hg^{2+}, leading to fluorescence quenching of QDs.

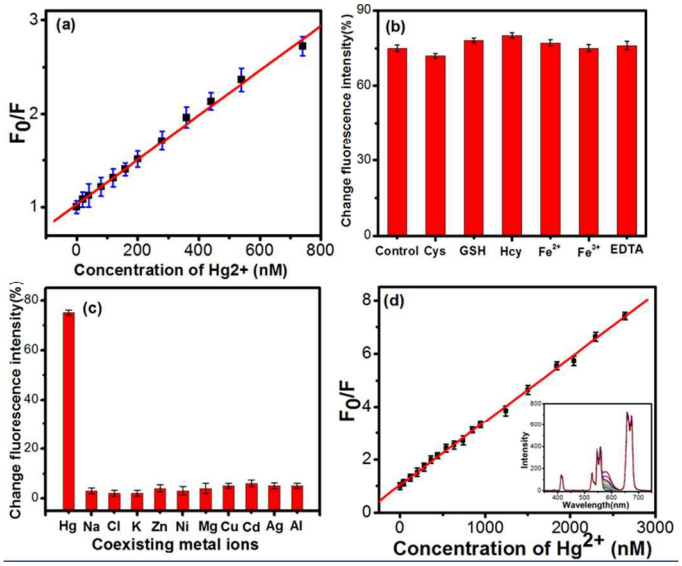

Fig.5 (a) Fluorescence intensity ratio of FRET sensor as a function of Hg^{2+} concentration detected in the buffer. F0 and F are the fluorescence intensities of QDs in the absence and presence of Hg2+, respectively. (b) Detection of Hg^{2+} in absence and presence of interference in human serum, including GSH, Cys, Hcy, Fe^{2+}/Fe^{3+}, and EDTA. (c) Detection selectivity for Hg^{2+}. Concentration of all ions was 0.5 mM. (d) Fluorescence intensity ratio of FRET sensor as a function of Hg^{2+} concentration detected in human serum (inset: FRET spectra of bioassay experiments detected in human serum with addition of various Hg^{2+} concentrations).

To evaluate the sensitivity of this method, the fluorescence

intensities of PBS buffer containing UCNPs, QDs and different amounts of Hg^{2+} were monitored. The extent of fluorescence quenching of QDs was dependent on the concentration of Hg^{2+}, as shown in Fig. 5(a). The fluorescence quenching is best described by the Stern–Volmer equation:[32]

$$F_0/F = 1 + K[Q],$$

where F_0 and F are the fluorescence intensities of QDs in the absence and presence of Hg^{2+}, respectively, [Q] is the mercury-ion concentration, and K is the Stern–Volmer constant. The calibration plot showed a good linear relationship in the 20–800 nM range (R=0.995), and K was determined to be 2.63 μM^{-1}.

Because interference from glutathione (GSH), cysteine (Cys) and homocysteine (Hcy) in human serum may influence Hg^{2+} detection, the anti-interference performance of the biosensor was measured. Fig. 5(b) shows the response of 1 μM Hg^{2+} in the absence (control) and presence of 1mM GSH, Cys, Hcy, Fe^{2+}/Fe^{3+}, and EDTA in the buffer, respectively. Adding each material did not significantly influence Hg^{2+} detection, which illustrates the biosensor's excellent anti-interference performance.

To estimate the selectivity of the FRET probe for Hg^{2+} detection, Mg^{2+}, K^+, Na^+, Cl^-, Zn^{2+}, Cu^{2+}, Cd^{2+}, Ag^+, Al^{3+} and Ni^{2+} were investigated along with Hg^{2+}. As shown in Fig. 5(c), only Hg^{2+} led to a dramatic change of fluorescence intensity, and no significant fluorescence intensity variation was found with the presence of other ions. Interfering ions exhibited low selectivity coefficients in the range of 0.024–0.159. These results clearly demonstrate the great selectivity of the biosensor for the target ion.

Because of superior sensitivity, selectivity, and anti-interference performance of our FRET probe in the buffer solution, we explored its capability to detect Hg^{2+} in human serum (0.1 g/mL). As shown in the Fig. 5(d) inset, upon addition of Hg^{2+} ions, the emission from 570 to 630 nm of QDs decreased continuously in intensity, but without a peak shift. Meanwhile, the emission intensity of Er^{3+} in the range of 400–570 nm and 640–720 nm did not change. The decay dynamics for $^4S_{3/2}$-$^4I_{15/2}$ transition processes of Er^{3+} with different Hg^{2+} concentration were further investigated. As shown in Fig. S9, all the dynamic curves exhibited exponential decay process, it can be seen that the decay rates for $^4S_{3/2}$-$^4I_{15/2}$ of Er^{3+} almost unchanged. The results indicate that Hg^{2+} should not affect the luminescence of Er^{3+} and the ET process from Er^{3+} to QDs, instead, affect the luminescence of QDs. The carboxyl capping layer was crucial for CdTe QD luminescent efficiency and water stability. Thus, as adding the Hg^{2+} ions, the surface states of QDs changed with the addition of Hg^{2+}, leading to fluorescence quenching of QDs. The calibration plot of F_0/F versus Hg^{2+} concentration in human serum (0.1 g/mL) showed a good linear relationship in the 10–2800 nmol/L range, as shown in Fig. 5(d). The plots are well described by the Stern–Volmer equation (R = 0.993), and K was determined to be 2.57 μM^{-1}. Fluorescence intensity ratio of FRET sensor as a function of Hg^{2+} concentration detected in human serum (0.15 g/mL) was further measured, as shown in Fig. S10. It can be seen that the calibration plot of F_0/F versus Hg^{2+} concentration in human serum (0.15 g/mL) showed a good linear relationship in the 10–2800 nmol/L range. The plots are well described by the Stern–Volmer equation (R = 0.994), and K was determined to be 2.60 μM^{-1}. The results were similar to those detected in the PBS buffer. The results indicate that our FRET probe has superior sensitivity in different concentration of human serum. The theoretical detection limit was evaluated using 3σ/S and determined to be 15 nM in human serum of 0.1 g/mL and 17 nM in human serum of 0.15 g/mL, where σ represents the standard deviation of the blank signal. The σ can be calculated as[13]

$$\sigma = \sqrt{\frac{\sum(F_n - \bar{F})^2}{n}},$$

where F_n represents the luminescence intensity for the nth time, F represents the average value of the luminescence intensity for multiple measurements, and S is the slope of the calibration plot. Many vital organs such as human heart, kidney, stomach and intestines can be poisoned and damaged when the Hg^{2+} concentration reaches a level of 25 nM. As soon as the content of Hg^{2+} exceeds the standard, it can be detected by our system.

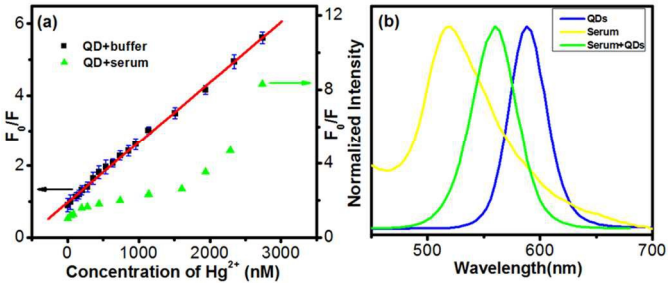

Fig.6 (a) Fluorescence intensity ratio of QDs-based sensor as a function of Hg^{2+} concentration detected in human serum and in buffer. (b) Emission spectra of QDs, serum and QDs with serum excited with 365 nm.

Actually, CdTe QDs probes can be used directly for the detection of Hg^{2+} in aqueous solution. In order to confirm that the present $NaYF_4$:Yb^{3+}, Er^{3+} UCNPs/CdTe QDs hybrid probes was superior to the single QD probes, Only CdTe QDs probes were used for Hg^{2+} detection, in buffer and human serum, respectively. Fig. 6(a) shows the calibration plot of F_0/F versus Hg^{2+} concentration for the CdTe QDs probes under 365 nm excitation. It can be seen that in the PBS solution, the calibration plot of F_0/F versus Hg^{2+} concentration show a good linear relationship in the range of 20-2800 nM, indicating that CdTe QDs also exhibit good performance of Hg^{2+} detection in the PBS buffer, the fluorescence spectra of QDs with addition of various Hg^{2+} concentrations was shown in Fig. S11. Unfortunately, the calibration plot of F_0/F versus Hg^{2+} concentration shows no linearity from 20 to 2800 nM in the serum. In order to clarify its origin, the emission spectra of the mixture of CdTe QDs and serum under the excitation of 365 nm were measured, as shown in Fig. 6(b). It can be seen that the emission band of the CdTe QDs locates at 590 nm, after the serum was added to the CdTe QDs, the

emission spectra of the mixture of QDs and serum under the excitation of 365 nm was measured, actually, the emission band of the QDs still locates at 590nm, meanwhile, the emission band of the serum locates at 520 nm under 365 nm excitation, leading to the emission spectra of the mixture of QDs and serum under the excitation of 365 nm blue-shifted from 590 nm to 555 nm comparing to the QDs emission, attributed to the spectra superposition of QDs and serum. After Hg^{2+} ions was added to the mixture of QDs and serum, the emission intensity of QDs weaken with the increase of Hg^{2+} ions concentration, while the emission intensity of serum remained virtually unaltered, leading to the fluorescence intensity ratio of the mixture of QDs and serum versus Hg^{2+} concentration shows no linearity from 20 to 2800 nM in human serum. This shows that the fluorescence of serum had great impact on the fluorescence of the mixture of CdTe QDs and serum, leading to no linearity in the serum. The serum emission is caused mainly by porphyrin, serum proteins, and carotenoids, as reported previously.[33]

Table 1 Comparison of different nanoparticle-based fluorescent probes for Hg^{2+} detection.

Fluorescence probes	Linear range (μM)	Detect limit (μM)	References
UCNPs/QDs	0.01-2.8	0.015	This work
Cysteine functionalized silver nanoparticles	0-55	0.065	34
DNA-functionalized gold nanoparticles	0.05-2.5	0.025	35
Carbon dots	0-2.69	1.3	36
Functionalized carbon dots	0.1-2.69	2.69	37
Polymer sensor	1-30	0.728	38

Compared to five other reported methods based on different fluorescence probes, the proposed method shows better linear range and sensitivity as shown in Table. 1. Liu *et al.* reported a sensor synthesized with rhodamine derivative covalently liked onto grapheme quantum dots for Hg^{2+} detection in Hela cells, the sensor was cell permeable and could be used for monitoring Hg^{2+} in living cells, however, the best linear response concentration range of Hg2+ in the sensor was from 0.6 to 12 μM with a correlation coefficient of 0.992, and the detection limit was estimated to be 0.23μM.[39] It can be concluded that the system we established is a comparatively facile method to detect Hg^{2+} ions in human serum.

5 Conclusions

In conclusion, we developed a new type of mercury biosensor based on FRET from $NaYF_4$:Yb^{3+}, Er^{3+} UCNPs to the CdTe QDs, which overcomes the lack of NIR-excitable probes for mercury ions. The sensor can be used for mercury-ion sensing both in the PBS buffer and in serum with comparable performance, proving that the biosensor is capable of overcoming autofluorescence from serum excitation due to visible light. When applied to detect mercury ions in human serum, the sensor had a good linear relationship (R = 0.996), and a low detection limit (15 nM), thereby easily detecting the 25 nM safety limit of mercury in the blood. Thus, the sensor we designed has great potential for real applications in mercury detection in biological and analytical fields.

Acknowledgements

This work was supported by the Major State Basic Research De velopment Program of China (973 Program) (no. 2014CB643506), the National Natural Science Foundation of China (Grant no. 113741 27, 11304118, 61204015, 81201738, 81301289, 61177042, and 1117 4111), the program of Chang Jiang Scholars and Innovative Research Team in University (no. IRT13018), the Graduate Innovation Fund of Jilin University (no. 2015064)

Notes and references

[a]State Key Laboratory on Integrated Optoelectronics, College of Electronic Science and Engineering, Jilin University, 2699 Qianjin Street, Changchun 130012, China.

[b]College of Physics, Jilin University, 2699 Qianjin Street, Changchun 130012, China.

Email: songhw@jlu.edu.cn, whan@jlu.edu.cn.

1 T. W. Clarkson, L. Magos and G. J. Myers, *N. Engl. J. Med*., 2003, **349**, 1731−1737.

2 E. M. Nolan and S. J. Lippard, *Chem. Rev.*, 2008, 108, 3443−3480.

3 H. N. Kim, W. X. Ren, J. S. Kim and J. Yoon, *Chem. Soc. Rev.*, 2012, **41**, 3210−3244.

4 T. W. Clarkson and L. Magos, *Crit. Rev. Toxicol.*, 2006, **36**, 609−662.

5 D. S. Zou, D. S. Zhai, H. Y. Sun and K. Zhang, *Spectrochimica Acta Part A: Molecular and Biomolecular Spectroscopy*, 2014, **118**, 1062–1067.

6 D. Sánchez-Rodas, W. T. Corns, B. Chen and P. B. Stockwell, *J. Anal. At. Spectrom.* 2010, **25**, 933-946.

7 K. Leopold, M. Foulkes and P. J. Worsfold, *Anal. Chim. Acta*, 2010, **663**, 127–138.

8 J. Y. Pei, H. Zhu, X. L. Wang, H. C. Zhang and X. R. Yang, *Anal. Chim. Acta*, 2012, **757**, 63–68.

9 Q. Mu, Y. Li, H. Xu, Y. F. Ma, W. H. Zhu and X. H. Zhong, *Talanta*, 2014, **119**, 564–571.

10 S. J. Liu, Z. J. Shi, W. J. Xu, H. R. Yang, N. Xi, X. M. Liu, Q. Zhao and W. Huang, *Dyes Pigments*, 2014, **103**, 145-153.

11 W. J. Yan, Y. L. Wang, H. Zhuang and J. H. Zhang, *Biosens. Bioelectron.* 2015, **68**, 516–520.

12 X. J. Ding, L. B. Qu, R. Yang, Y. C. Zhou and J. J. Li, *Luminescence,* 2015, **30**, 465–471.

13 S. Xu, S. H. Xu, Y. S. Zhu, W. Xu, P. W. Zhou, C. Y. Zhou, B. Dong and H. W. Song. *Nanoscale*, 2014, **6**, 12573–12579.

14 J. H. Zhang, Z. D. Hao, J. Li, X. Zhang, Y. S. Luo and G. H. Pan, *Light. Sci. Appl.*, 2015, **4**, e239.

15 A. Bednarkiewicz, M. Nyk, M. Samoc and W. Strek, *J. Phys. Chem. C*, 2010, **114**, 17535–17541.

16 L. Q. Xiong, Z. G. Chen, Q. W. Tian, T. Y. Cao, C. J. Xu and F. Y. Li, *Anal. Chem.*, 2009, **81**, 8687–8694.

17 M. Nyk, R. Kumar, T. Y. Ohulchanskyy, E. J. Bergey and P. N. Prasad, *Nano Lett.*, 2008, **8**, 3834.

18 M. X. Yu, F. Y. Li, Z. G. Chen, H. Hu, C. Zhan, H. Yang and C. H. Huang, *Anal. Chem.,* 2009, **81**, 930–935.

19 Y. Park, J. H. Kim, K. T. Lee, K. S. Jeon, H. B. Na, J. H. Yu, H. M. Kim, N. Lee, S. H. Choi and S. B. Aik, *Adv. Mater.*, 2009, **21**, 4467–4471.

20 L. H. Fischer, G. S. Harms and O. S. Wolfbeis, *Angew. Chem. Int. Ed.* 2011, **50**, 4546–4551.

21 D. E. Achatz, R. J. Meier, L. H. Fischer and O. S. Wolfbeis, *Angew. Chem. Int. Ed.* 2011, **50**, 260–263.

22 H. S. Mader and O. S. Wolfbeis, *Anal. Chem.*, 2010, **82**, 5002–5004.

23 Y. Liu, M. Chen, T. Y. Cao, Y. Sun, C. Y. Li, Q. Liu, T. Yang, L. M. Yao, W. Feng and F. Y. Li, *J. Am. Chem. Soc.*, 2013, **135**, 9869.

24 S. J. Wu, N. Duan, Z. Shi, C. C. Fang and Z.P. Wang, *Talanta*, 2014, **128**, 327–336.

25 Q. Liu, J. J. Peng, L. N. Sun and F. Y. Li, *ACS Nano*, 2011, **5**, 8040-8048.

26 F. Wang and X. G. Liu, *J. Am. Chem. Soc.*, 2008, **130**, 5642.

27 L. H. Jin, L. Shang, J. F. Zhai, J. Li and S. J. Dong, *J. Phys. Chem. C*, 2010, **114**, 803–807.

28 S. B. Cui, Y. S. Zhu, W. Xu, P. W. Zhou, L. Xia, X. Chen, H. W. Song, W. Han, *Dalton. Trans.*, 2014, **43**, 13293–13298.

29 T. T. Li, Z. N. Wu, T. T. Huang, J. l. Liu, L. Rong, S. J. Lan, Z. X. Guo, H. Zhang, B. Yang, *RSC Adv.*, 2015, **5**,48024–48030.

30 R. Gill, M. Zayats, I. Willner, *Angew. Chem. Int. Ed.*, 2008, **47**, 7602.

31 Y. Kobayashi, L. Y. Pan, N. Tamai, *J. Phys. Chem. C*, 2009, **113**, 11783.

32 E. M. Ali, Y. G. Zheng, H. H. Yu, J. Y. Ying, *Anal. Chem.,* 2007, **79**, 9452.

33 J. Yu, J. W. Meng, Y. Li, J. Ma and R. E. Rong, *Spectrosc. Spec. Anal.*, 2004, **24**, 981.

34 L. Shang, J. Yin, J. Li, L. Jin, S. Dong, Biosens. Bioelectron., 2009, 25,269-274.

35 C. W. Liu, C. C. Huang, H. T. Chang, Langmuir., 2008, 24, 8346-8350.

36 H. M. R. Goncalves, A. J. Duarte, J. C. G. E. daSilva, Biosens. Bioelectron., 2010, 26, 1302-1306.

37 H. Goncalves, P. A. S. Jorge, J. R. A. Fernandes, J. C. G. E. daSilva, Sens. Actuators B Chem. 2010, 145, 702-707.

38 J. Li, Y. Wu, F. Song, G. Wei, Y. Cheng, C. Zhu, J. Mater. Chem. 2012, 22, 478-482.

39 M. P. Liu, T. Liu, Y. Li, H. Xu , B. Z. Zheng , D. M. Wang, J. Du, D. Xiao, Talanta, 2015, **143**, 442-449

